



# Atomic structures of grain boundaries for Si and Ge: A simulated annealing method with artificial-neural-network interatomic potentials

Tatsuya Yokoi <sup>a,\*</sup>, Hirotaka Kato <sup>a</sup>, Yu Oshima <sup>a</sup>, Katsuyuki Matsunaga <sup>a,b</sup>

<sup>a</sup> Department of Materials Physics, Nagoya University, Nagoya, 464-8603, Japan

<sup>b</sup> Nanostructures Research Laboratory, Japan Fine Ceramics Center, Nagoya, 456-8587, Japan



## ABSTRACT

To accurately predict low-energy structures for symmetric tilt grain boundaries (GBs) in Si and Ge, artificial-neural-network (ANN) interatomic potentials are constructed and are combined with a simulated annealing (SA) method based on molecular dynamics simulations. The ANN-driven SA method is demonstrated to predict GB structures that are in good agreement with previous electron microscopy observations, without prior knowledge about their atomic configurations. Their GB energies also reasonably agree with density-functional-theory (DFT) calculations. By contrast, a conventional empirical potential fails to predict those GB structures. For misorientation angles  $2\theta \geq 93.37^\circ$ , the lowest-energy structures are found to contain atomic configurations that cannot be reproduced by one repeat unit of the perfect crystal along the tilt axis. Such GB structures cannot be obtained using the  $\gamma$ -surface method, although it is most commonly used for exploring low-energy GB structures. These results highlight the importance of using simulation cells with multiple repeat units along the tilt axis and of performing the SA method with high-accuracy interatomic potentials transferable to GBs.

## 1. Introduction

Polycrystalline semiconductors meet many current and potential applications for electronic, photovoltaic and thermoelectric materials, due to low-cost, large-scale fabrication. In such materials, grain boundaries (GBs) inevitably exist and often have both beneficial and detrimental effects on target material properties. For instance, GBs provide segregation sites for impurities [1–5], which act as recombination centers, whereas they can be utilized to getter unwanted impurities [6,7]. GBs are also known to effectively reduce lattice thermal conductivity by scattering phonons and restricting their effective mean free paths [8–10]. Such effects primarily arise from GB atomic structures distinct from the perfect crystal, which vary with individual GBs as indicated by electron microscopy observation [3,4,11–13]. For fabrication of high-performance polycrystalline semiconductors, it is thus required to reveal atomic structures and physical properties of crystallographically various GBs and ultimately to obtain the fundamental knowledge about general GBs.

For this purpose, density-functional-theory (DFT) calculations and empirical-potential simulations have been performed extensively for semiconductors [14–17], as well as metals [18–21] and ceramics [22–24]. It has been indicated that the crystallographically same GBs often exhibit different atomic configurations with a wide spectrum of GB energies [14,16,25–27]. This is because the potential energy surface at a

GB is generally more complicated than its perfect crystal, thereby having many local minima in configuration space. Examples include even low- $\Sigma$  GBs for simple fcc [26] and bcc metals [25,27], for which new lower-energy structures were recently discovered. For a critical example of semiconductor GBs, DFT analysis on the  $\Sigma 3(112)$  symmetric tilt GB (STGB) in CdTe demonstrated that an asymmetric structure with respect to the GB plane is energetically more favorable than a commonly used symmetric one [28]; furthermore, the asymmetric structure has no deep defect level in the band gap while the symmetric one shows a clear deep level [28]. This highlights the importance of exploring low-energy structures, and more importantly, of determining the lowest-energy structure for a GB.

However, it is still challenging to explore low-energy GB structures by using DFT calculations because GB simulation cells often require many atoms, leading to large computational cost. Even for low- $\Sigma$  tilt STGBs in simple cubic systems, low-energy structures were found to have complex atomic configurations with greater periodicities along the tilt axis than that of the conventional cell of the perfect crystal [25–27], which require at least several hundreds of atoms. Additionally, such complex GB structures are often inaccessible with the  $\gamma$ -surface method based on structural relaxation, although this method is most commonly used [18–22]. Instead, one requires more expensive methods, e.g. using evolutionary algorithm methods with many structural-relaxation calculations [16,25–27,29] and simulated annealing (SA) methods with

\* Corresponding author.

E-mail address: [yokoi@mp.pse.nagoya-u.ac.jp](mailto:yokoi@mp.pse.nagoya-u.ac.jp) (T. Yokoi).

long-time molecular dynamics (MD) simulations [24,30]. Although empirical potentials enable performing these methods with low computational cost, their empirical parameters typically are not fitted to atomic environments at GBs. This can lead to critical errors in prediction of low-energy GB structures [31,32]. Furthermore, empirical potentials are essentially based on physically-derived analytic functions with simple functional forms, which also leads to the limited transferability to GBs.

Recently, machine-learning interatomic potentials have become as a powerful approach to achieve both low computational cost and high accuracy [33–39]. In this approach, machine-learning models with many adjustable parameters are trained using a large amount of DFT data, and they can in turn interpolate the potential energy surface within the Born-Oppenheimer approximation. The current major approaches are based on artificial-neural-networks (ANN) [33,35,36] and Gaussian process approximations [34,37]. Their excellent transferability has been demonstrated for not only perfect crystals but also lattice defects such as point defects [40–44], surfaces [44–46] and dislocations [47–50]. To our knowledge, however, their applicability to the determination of low-energy GB structures still remains unclear, although a few studies constructed machine-learning potentials and combined them with the  $\gamma$ -surface method to examine their ability to predict GB energies [51–53]. To explore possible low-energy GB structures, more expensive methods are often desired as mentioned above.

The present study constructs ANN potentials for predicting low-energy GB structures. Here, Si and Ge with the diamond structure are chosen as their GBs are technologically and scientifically important. The ANN potentials are combined with a SA method based on MD simulation to determine the lowest-energy structures for STGBs. The obtained structures and their GB energies are then compared with previous experimental observations and DFT calculations in order to examine the prediction ability of the ANN-based simulations. The  $\gamma$ -surface method is also performed to confirm its limitation to finding the lowest-energy GB structures.

## 2. Computational methods

### 2.1. DFT calculation

DFT calculations with the projected augmented wave (PAW) method [54,55] were performed using the Vienna *Ab initio* Simulation Package (VASP) [56,57]. The electrons in the 3s and 3p orbitals for Si and in the 3d, 4s and 4p orbitals for Ge were assumed to be valence electrons. The exchange-correlation energy was calculated using a revised version of the generalized gradient approximation formulated by Perdew, Burke and Ernzerhof (GGA-PBEsol) [58]. The energy cutoff was chosen to be 500 eV for both Si and Ge. The convergence criterion in terms of total energy was set to  $10^{-6}$  eV. To generate training datasets, DFT-MD simulations based on the Parrinello-Rahman dynamics with the Langevin thermostat [59,60] were also performed using both NVT and NPT conditions with a time step of 2 fs. For  $k$ -point sampling,  $6 \times 6 \times 6$  meshes were employed to a cubic unit cell for both Si and Ge.

### 2.2. ANN potential

This work implemented two ANN potentials with two hidden layers each having 48 nodes. At the input layer, 8 two-body and 24 three-body symmetry functions [36] were used as atomic descriptors to encode a given atomic environment, with cutoff distances of 6 and 6.5 Å for Si and Ge, respectively. Their hyperparameters were empirically determined as listed in the supplementary material, and the same hyperparameters were used for Si and Ge. The hyperbolic tangent was used as an activation function.

For DFT training datasets of the ANN potentials, various reference structures were initially constructed, including intrinsic point defects, surfaces and GBs. Using the reference structures, training datasets were

generated in the following two ways. First, multiple different structures were constructed from a reference structure by randomly changing its cell dimensions and atomic positions. The constructed structures were structurally relaxed for up to 20 iterations, and snapshots in this calculation were contained in the training datasets. Second, DFT-MD simulations were performed for several hundreds of steps at temperatures up to 2800 and 2400 K for Si and Ge, respectively, and snapshots were also used for ANN training. The training datasets contained 78,000 energies and 5,370,051 atomic forces for Si and 71,500 energies and 4,824,615 atomic forces for Ge. Details of the training datasets are summarized in Table 1. An extended Kalman filter with weighted least squares [61] was employed to train the ANN potentials.

### 2.3. SA method with ANN potential

The ANN potentials were then combined with a SA method based on MD simulation and were applied to eight STGBs with the  $\bar{[1}10]$  tilt axis. The SA method utilizes energy fluctuation arising from lattice vibration, which enables escaping from local minima and also increases the probability of reaching the lowest-energy structure by sampling a wide range of configuration space. In this method, an MD simulation started at a high temperature, and then the temperature was linearly decreased with time step. After this MD simulation, the atomic positions were fully relaxed using the ANN potential, and its GB energy was calculated using the ANN potential and DFT calculations. It should be noted that a GB often has many local minima. Thus SA simulations were repeatedly performed by setting different initial velocity distributions and also generating multiple initial simulation cells with different rigid translations of two grains. Apart from the SA method, the  $\gamma$ -surface method with a nonlinear conjugate gradient algorithm was also performed using the ANN potentials to demonstrate its limitation to finding the lowest-energy structure of a GB. The details of simulation cells and computational conditions for the SA and  $\gamma$ -surface methods are given in the supplementary material.

Note that for an observed structure of the  $\Sigma 9(111)\parallel(115)/\bar{[1}10]$  asymmetric tilt GB (ATGB), the repeat-unit length along the  $\bar{[1}10]$  axis is twice that of the conventional cell of the perfect crystal [12]. Thus GB simulation cells with one and two repeat units of the perfect crystal along the tilt axis were used in the SA method, whose conditions are denoted by SA(1) and SA(2), respectively. It is also noted that the atomic density of the GB plane can be an important factor in determining the lowest-energy structure for a GB, as indicated for twist GBs in Si [62] and STGBs in bcc and fcc metals [25–27]. In our test calculations on  $[001]$ -axis STGBs, however, GB structures without variation in atomic density showed the lowest GB energies. This work thus assumed that variation in atomic density of the GB plane was also absent for the  $\bar{[1}10}$ -axis STGBs examined. This assumption is probably valid because the obtained lowest-energy structures of the  $\Sigma 9(221)$ ,  $\Sigma 3(111)$ ,  $\Sigma 3(112)$  and  $\Sigma 9(114)$  STGBs are in quantitatively agreement with scanning transmission electron microscopy (STEM) observations [3,63], as indicated by Figs. 3 and 5 and S2 in the supplementary material.

The SA(2) method with the Tersoff potential [64,65] was also performed to examine its ability to predict low-energy GB structure for the  $\Sigma 9(114)$  STGB. Classical molecular simulations based on the Tersoff potential were performed using the LAMMPS [66] and GULP codes [67].

## 3. Results and discussion

For Si, the mean absolute errors (MAEs) for the training datasets are calculated to be 4.9 meV/atom and 111 meV/Å for the total energy and atomic force, respectively. The ANN potential for Ge shows similar values, with 4.0 meV/atom and 84 meV/Å. These values are in the same level as those in the literature [52,68,69]. The present ANN potentials are thus expected to be able to perform structural relaxation and MD simulations with reasonable accuracy if a given atomic environment is

**Table 1**

Training datasets for Si and Ge.  $N_{\text{atom}}$ ,  $N_{\text{str}}$ ,  $N_{\text{force}}$  denote the number of atoms in one simulation cell, the number of simulation cells and the number of atomic forces in each of the training datasets, respectively.  $N_{\text{str}}$  is the same as the number of total energies used for ANN training. The training datasets labeled as “Structural relaxation” and “MD” were generated using structural relaxation calculations and MD simulations based on DFT calculations, respectively, as mentioned in the main text.

Structure		Si			Ge		
		$N_{\text{atom}}$	$N_{\text{str}}$	$N_{\text{force}}$	$N_{\text{atom}}$	$N_{\text{str}}$	$N_{\text{force}}$
Single crystal	Structural relaxation	8–71	13000	548022	7–71	5400	146793
	MD	60–64	16000	1488000	62–67	8000	769500
(100) surface	Structural relaxation	14	1500	31500	16	2800	67200
	MD	64	4000	384000	62–67	4000	382500
(110) surface	Structural relaxation	10	1500	22500	12	2800	50,400
	MD	46	1500	103500	12	2800	50400
(112) surface	Structural relaxation	46	1500	103500	24	2800	100800
	MD	46	1500	103500	24	2800	100800
$\Sigma 5(310)/[001]$	Structural relaxation	39–41	2300	136596	38–40	2300	135900
STGB $\Sigma 5(210)/[001]$ STGB	MD	40	3500	210000	40	4000	240,000
	Structural relaxation	39–41	2300	136800	38–40	2300	135816
$\Sigma 3(112)/[\bar{1}10]$	MD	40	3500	210000	40	4000	240000
	Structural relaxation	39–40	3000	175176	48	1900	136800
STGB $\Sigma 9(221)/[\bar{1}10]$ STGB	MD	40	3500	210000	48	4000	288000
	Structural relaxation	49–51	2400	178704	52	2600	202,800
$\Sigma 9(114)/[\bar{1}10]$	MD	50	3500	262500	52	4000	312000
	Structural relaxation	72	1500	162,000	69–72	1400	135900
STGB $\Sigma 11(113)/[\bar{1}10]$	MD	72	3500	378000	72	4000	432000
	Structural relaxation	44	1500	99000	41–44	2300	144777
STGB $\Sigma 19(331)/[\bar{1}10]$	MD	44	3500	231000	44	4000	264000
	Structural relaxation	39–41	1500	89253	73–76	1100	122190
STGB	MD	40	3500	210000	76	4000	456000
Total			78000	5370051		71500	4824615

sufficiently covered by the training datasets. The ANN potentials predict that the lowest-energy lattice constants are 5.436 and 5.672 Å for the conventional cells of Si and Ge, respectively, which are identical to the DFT values (5.436 Å for Si and 5.673 Å for Ge).

Fig. 1 shows the correlation between ANN and DFT GB energies for all GBs examined. Each data point in this figure corresponds to GB energies obtained by the SA(2) method based on the ANN potential and the subsequent DFT single-point calculation (i.e., total-energy calculation without structural optimization) with respect to the same GB structure.

Thus if the ANN potential accurately predicts the DFT value for a GB structure, its data point resides close to the diagonal line. It is found that most of the data points ranging from low to high GB energies are distributed near the diagonal line. This indicates that the present ANN potentials accurately distinguish between low and high-energy states for GBs of both Si and Ge, enabling us to explore their low-energy structures with reasonable accuracy. Note that the data point indicated by the arrow in Fig. 1(a) involves a large deviation. It corresponds to the  $\Sigma 3(111)$  STGB, which consists of a coherent twin structure [3]. The

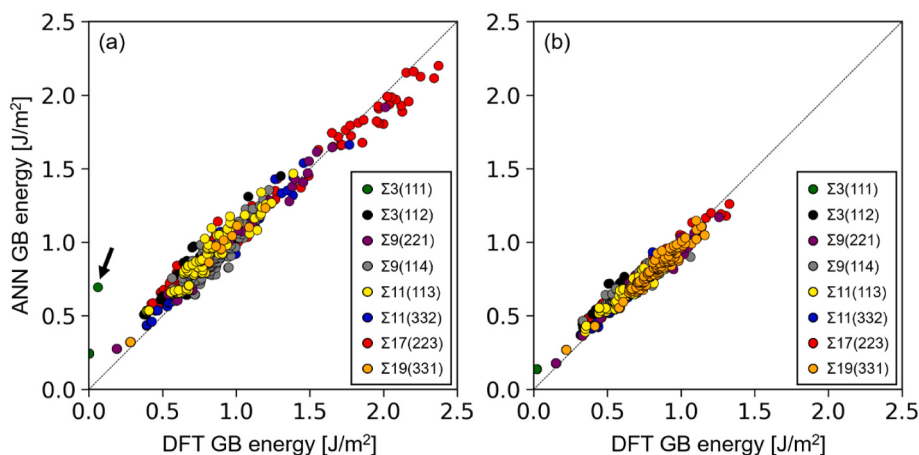


**Fig. 1.** Correlation between the ANN and DFT GB energies for (a) Si and (b) Ge. These values were obtained from the GB structures for the SA(2) method with the ANN potential.

present training datasets do not contain this special STGB, leading to this large deviation, although the ANN potential still accurately predicts the coherent twin structure (see the supplementary material). Containing this STGB in the training datasets will further improve the prediction ability of the ANN potential with respect to GB energy.

Initially, the  $\Sigma 9(114)$  STGB for Si is discussed as a previous electron microscopy observation reported its atomic configuration [3], and thus a direct comparison can be made between the experimental image and our calculated structure. Fig. 2(a) shows ANN GB energies for this STGB, along with those obtained by DFT single-point calculations for the corresponding ANN-derived GB structures. It is found that the SA(2) provides the lowest-energy structure, with a GB energy of  $0.52 \text{ J/m}^2$ . This structure also has the lowest GB energy of  $0.39 \text{ J/m}^2$  in the DFT level. The ANN GB energy is thus reasonably in agreement with the DFT value, although the ANN potential slightly overestimates the DFT value by  $0.13 \text{ J/m}^2$ .

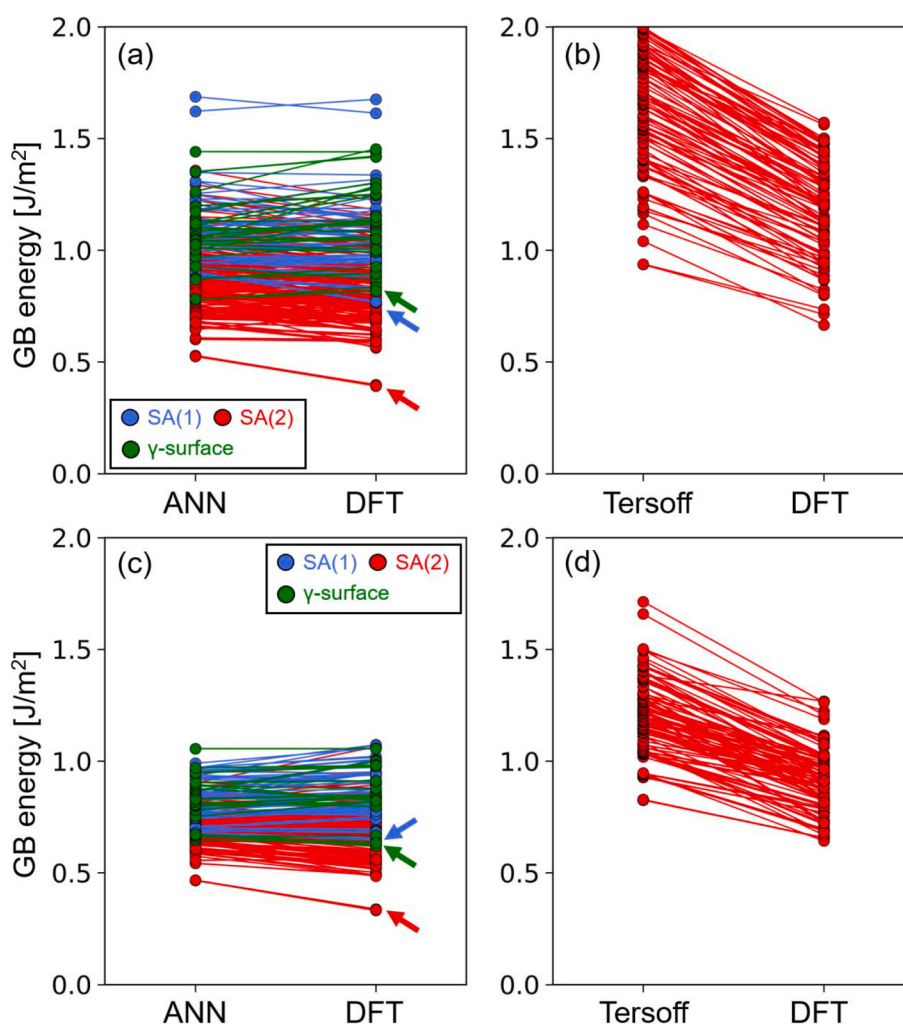
Fig. 2(a) also indicates that the lowest-energy structure for the  $\gamma$ -surface method has a higher GB energy ( $0.82 \text{ J/m}^2$ ) than that for the SA(2) method, as indicated by the green arrow, and also it is energetically higher than many structures for the SA(2). This highlights the limitation of the  $\gamma$ -surface method in prediction of low-energy GB structures. The SA(1) also incorrectly predicts a higher energy structure to be the lowest-energy one, as indicated by the blue arrow. This is because the lowest-energy structure for the SA(2) has an atomic configuration that cannot be reproduced with one repeat unit of the conventional cell of the perfect crystal along the  $\bar{[1}10]$  axis, as will be shown in Fig. 3. Fig. 2(c) shows that for Ge, only the SA(2) can provide

the lowest-energy structure by DFT, similar to the case of Si.

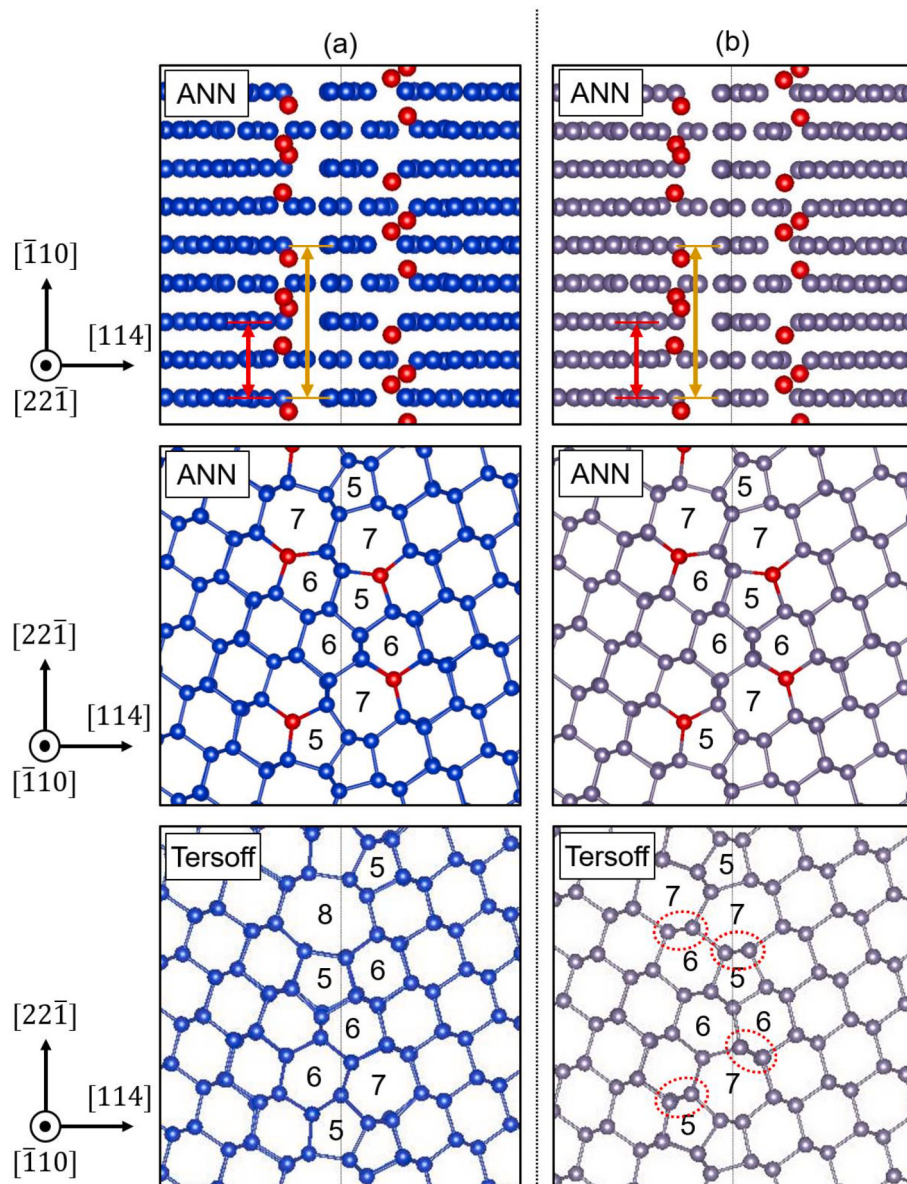
A comparison of Fig. 2(a)–(b) indicates that the DFT GB energy of the lowest-energy structure predicted by the Tersoff potential is higher by  $0.28 \text{ J/m}^2$  than that of the ANN lowest-energy structure. Indeed, the Tersoff and ANN GB structures are different as shown later in Fig. 3. Additionally, the Tersoff structures tend to exhibit higher GB energies than those for the SA(2) based on the ANN potential. The Tersoff potential is thus likely to be difficult to use for exploring low-energy GB structures, and more importantly, for predicting the lowest-energy GB structures.

Fig. 3 displays the lowest-energy structure obtained from the SA(2) for  $\Sigma 9(114)$ . For the red atoms, it can be seen that the periodicity along the  $\bar{[1}10]$  axis is doubled, as indicated by the double-headed arrows. This trend is similar to the  $\Sigma 9(111)\parallel\bar{[1}10]$  ATGB reported in the literature [12]. When projected along the  $\bar{[1}10]$  axis (see the middle picture in Fig. 3(a)), the ANN structure contains three five- and three seven-membered rings in one period along the  $[22\bar{1}]$  axis. This structural unit is in excellent agreement with a previous STEM image [3]. Importantly, the ANN potential for Si successfully predicts this structure without any assumption of the previous STEM image, which will also enable us to predict the lowest-energy structures for other GBs even without experimental results. Although there is no experimental observation on the  $\Sigma 9(114)/\bar{[1}10]$  STGB for Ge, its structural unit is the same as that for Si. It is thus likely that the STGB for Ge also exhibits the greater periodicity along the  $\bar{[1}10]$  axis.

As shown in the bottom pictures in Fig. 3, the Tersoff structures are



**Fig. 2.** GB energies of the  $\Sigma 9(114)/\bar{[1}10]$  STGB for (a) the ANN potential for Si, (b) the Tersoff potential for Si, (c) the ANN potential for Ge and (d) the Tersoff potential for Ge. In Fig. 1(a) and (c), the data points for the SA(1), SA(2) and  $\gamma$ -surface methods are indicated in blue, red and green, respectively. For all panels, the data points on the left side indicate the ANN/Tersoff GB energies, and those on the right side are GB energies for the respective GB structures obtained by DFT single-point calculations. Two points connected with a line are obtained from the same simulation cell.



**Fig. 3.** Lowest-energy atomic configurations obtained from the ANN potentials (top and middle panels) and the Tersoff potentials (bottom panels) for the  $\Sigma 9(114)/[110]$  STGB in (a) Si and (b) Ge.

different from the ANN ones. For Si, it contains two five-, one seven- and one eight-membered rings. For Ge, it contains the same number of five- and seven-membered rings as the ANN structure; however, its column positions at the GB are dissimilar to those for the ANN structure, as marked by the dashed red circles in the bottom picture in Fig. 3(b).

The other GBs are also examined using the SA(1), SA(2) and  $\gamma$ -surface methods with the ANN potential. Fig. 4 displays their lowest GB energies as a function of misorientation angle of two grains,  $2\theta$ . For  $2\theta \leq 50.48^\circ$ , the GB energies are the same between the three methods. Indeed, their lowest-energy structures are found to be the same and are in agreement with previous experimental and theoretical results [3,17], as displayed in the supplementary material. However, the SA(2) again shows the lowest GB energies for  $2\theta \geq 93.37^\circ$  for both Si and Ge. These trends are also observed for the DFT values as indicated by the dash lines. This demonstrates that in a certain range of  $2\theta$ , the  $\gamma$ -surface method fails to reach the lowest-energy structures due to its limited ability to search configuration space. The SA(2) lowest-energy structure is also inaccessible with the SA(1), which used simulation cells with one repeat unit of the perfect crystal along the tilt axis. The lowest-energy structures

predicted from the SA(2) method are all provided in the supplementary material.

Note that the ANN GB energies overestimate the corresponding DFT values for  $2\theta \geq 93.37^\circ$ , as is the case for the  $\Sigma 3(111)$  STGB. In addition, there exist some discrepancies between the ANN and DFT values, e.g., the relative GB energies of the  $\Sigma 11(113)$  and  $\Sigma 9(114)$  STGBs. These discrepancies probably arise from the fact that the training datasets contained GB simulation cells only with one repeat unit of the perfect crystal along the  $[110]$  axis, while the lowest-energy GB structures obtained from the SA(2) method have two repeat units, as indicated for the  $\Sigma 3(112)$ ,  $\Sigma 9(114)$ ,  $\Sigma 11(113)$  and  $\Sigma 17(223)$  STGBs in Figs. 3 and 5. These GB structures essentially involve specific atoms that move along the  $[110]$  axis and create new bonds between these atoms, as indicated by the red atoms. Such distinct atomic environments probably are not included in the training datasets, due to the limited size of the simulation cells contained, as mentioned above. Although the origin of the overestimation has not been identified so far, whether overestimation or underestimation occurs is probably dependent on training datasets used, rather than an inherent feature of GBs. A direct way to improve the ANN

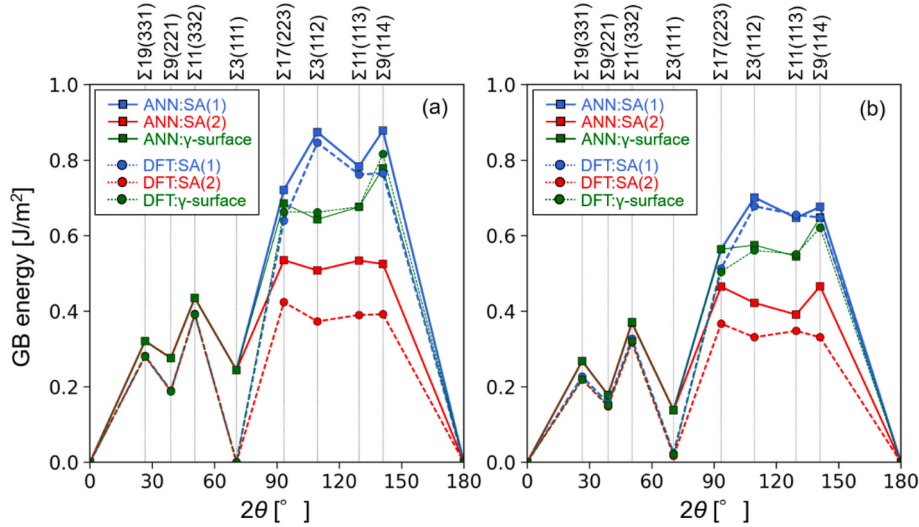


**Fig. 4.** GB energy as a function of misorientation angle of two grains ( $2\theta$ ) for STGBs with the  $[110]$  tilt axis in (a) Si and (b) Ge. The values of the SA(1), SA(2) and  $\gamma$ -surface methods are indicated in blue, red and green, respectively. The solid and dashed lines correspond to the ANN and DFT values, respectively.

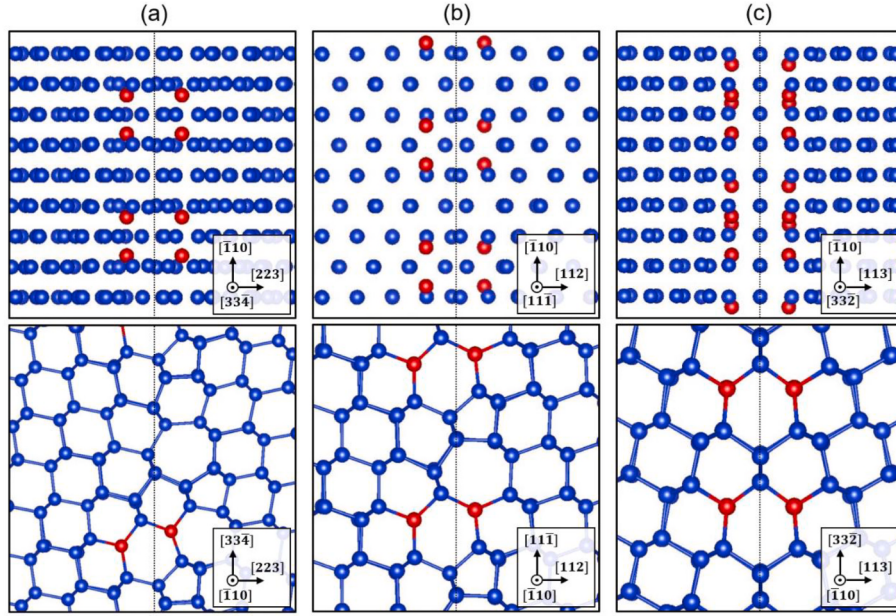


**Fig. 5.** Lowest-energy structures predicted from the SA(2) with the ANN potential for Si: (a)  $\Sigma 17(223)/[110]$ , (b)  $\Sigma 3(112)/[110]$  and (c)  $\Sigma 11(113)/[110]$ .

potential will be that GB simulation cells with two repeat units and with specific GB atoms as in the  $\Sigma 9(114)$  STGB are added to the training datasets, although more numbers of atoms are required to construct such simulation cells. In this respect, further improvement in training datasets will be desirable in future work.

Fig. 5 displays the SA(2) lowest-energy structures of the three STGBs for  $2\theta \geq 93.37^\circ$ . Similar to the  $\Sigma 9(114)$  STGB, their atomic configurations also cannot be reproduced using one repeat unit of the perfect crystal along the  $[\bar{1}10]$  axis, as indicated by the red atoms. It is expected that other STGBs for  $2\theta \geq 93.37^\circ$  also exhibit the same type of atomic configuration in their lowest-energy structures. The three STGBs in Ge are also found to have the same atomic configurations as those in Si, as shown in the supplementary material. This may suggest that the trend in the complex GB structures obtained is common for STGBs in Si and Ge. As mentioned earlier, the  $\Sigma 9(111)[(115)/[\bar{1}10]]$  ATGB was reported to have this type of atomic configuration [12]. It is thus anticipated that in order to explore low-energy structures for ATGBs in a certain range of

misorientation angle, one has to perform the SA(2) method with a high-accuracy interatomic potential.

#### 4. Conclusions

ANN potentials are constructed and are combined with a SA method based on MD simulation to accurately determine the lowest-energy structures for STGBs with the  $[\bar{1}10]$  rotational axis in Si and Ge. The ANN-based SA method demonstrates that in a certain range of misorientation angle, the lowest-energy GB structures exhibit complex atomic configurations whose repeat-unit length along the  $[\bar{1}10]$  axis is twice that of the perfect crystal. The SA method with the Tersoff potential fails to predict the lowest-energy structure of the  $\Sigma 9(114)$  STGB. The complex atomic configurations obtained are also inaccessible with the conventional  $\gamma$ -surface method. These results highlight the importance of performing SA method or other advancing methods with high-accuracy interatomic potentials, in order to accurately predict possible low-

energy structures for GBs in Si and Ge. This may also be true for other materials, which will be addressed in future research.

## Author Statement

T.Y. and H.K. conceived of the idea of this work, and performed the calculations. K.M. supervised this research, and Y.O. supported T.Y. and H.K. to carry out the analyses. T.Y. drafted this manuscript with support from K.M. and Y.O. All authors discussed the results for the final manuscript.

## Declaration of competing interest

The authors declare that they have no known competing financial interests or personal relationships that could have appeared to influence the work reported in this paper.

## Data availability

Data will be made available on request.

## Acknowledgements

This work was supported by JST-CREST (Grant Number JPMJCR17J1), JSPS KAKENHI (Grant Number JP19H05786, JP21K14405 and JP22H04508) and “Joint Usage/Research Center for Interdisciplinary Large-scale Information Infrastructures” in Japan (Project ID: jh220057). Molecular simulations in this work were partly performed using the facilities of the Supercomputer Center, the Institute for Solid State Physics, the University of Tokyo.

## Appendix A. Supplementary data

Supplementary data to this article can be found online at <https://doi.org/10.1016/j.jpcs.2022.111114>.

## References

- [1] J. Chen, T. Sekiguchi, D. Yang, F. Yin, K. Kido, S. Tsurekawa, Electron-beam-induced current study of grain boundaries in multicrystalline silicon, *J. Appl. Phys.* 96 (2004) 5490–5495.
- [2] A. Stoffers, O. Cojocaru-Mirédin, W. Seifert, S. Zaefferer, S. Riepe, D. Raabe, Grain boundary segregation in multicrystalline silicon: correlative characterization by EBSD, EBIC, and atom probe tomography, *Prog. Photovoltaics Res. Appl.* 23 (2015) 1742–1753.
- [3] Y. Ohno, K. Kutsukake, M. Deura, I. Yonenaga, Y. Shimizu, N. Ebisawa, K. Inoue, Y. Nagai, H. Yoshida, S. Takeda, Impact of local atomic stress on oxygen segregation at tilt boundaries in silicon, *Appl. Phys. Lett.* 109 (2016) 142105.
- [4] Y. Ohno, K. Inoue, K. Fujiwara, K. Kutsukake, M. Deura, I. Yonenaga, N. Ebisawa, Y. Shimizu, K. Inoue, Y. Nagai, H. Yoshida, S. Takeda, S. Tanaka, M. Kohyama, Recombination activity of nickel, copper, and oxygen atoms segregating at grain boundaries in mono-like silicon crystals, *Appl. Phys. Lett.* 110 (2017), 062105.
- [5] C.H. Liebscher, A. Stoffers, M. Alam, L. Lymparakis, O. Cojocaru-Mirédin, B. Gault, J. Neugebauer, G. Dehm, C. Scheu, D. Raabe, Strain-Induced asymmetric line segregation at faceted Si grain boundaries, *Phys. Rev. Lett.* 121 (2018), 015702.
- [6] S. Joonwichien, I. Takahashi, K. Kutsukake, N. Usami, Effect of grain boundary character of multicrystalline Si on external and internal (phosphorus) gettering of impurities, *Prog. Photovoltaics Res. Appl.* 24 (2016) 1615–1625.
- [7] D. Hu, S. Yuan, X. Yu, L. He, Y. Xu, X. Zhang, D. Yang, Grain boundary engineering of high performance multicrystalline silicon: control of iron contamination at the ingot edge, *Sol. Energy Mater. Sol. Cells* 171 (2017) 131–135.
- [8] G. Joshi, H. Lee, Y. Lan, X. Wang, G. Zhu, D. Wang, R.W. Gould, D.C. Cuff, M. Y. Tang, M.S. Dresselhaus, G. Chen, Z. Ren, Enhanced thermoelectric figure-of-merit in nanostructured p-type silicon germanium bulk alloys, *Nano Lett.* 8 (2008) 4670–4674.
- [9] Y. Lan, A.J. Minnich, G. Chen, Z. Ren, Enhancement of thermoelectric figure-of-merit by bulk nanostructuring approach, *Adv. Funct. Mater.* 20 (2010) 357–376.
- [10] Z. Wang, J.E. Alaniz, W. Jang, J.E. Garay, C. Dames, Thermal conductivity of nanocrystalline silicon: importance of grain size and frequency-dependent mean free paths, *Nano Lett.* 11 (2011) 2206–2213.
- [11] J.-L. Rouvière, F. Lançon, O.H. Duparc, Atomic structures of Si and Ge  $\Sigma = 13$  [001] tilt grain boundaries studied by high-resolution electron microscopy and atomic simulations, *Philos. Mag. A* 93 (2013) 1230–1249.
- [12] A. Stoffers, B. Ziebarth, J. Barthel, O. Cojocaru-Mirédin, C. Elsässer, D. Raabe, Complex nanotwin substructure of an asymmetric  $\Sigma 9$  tilt grain boundary in a silicon polycrystal, *Phys. Rev. Lett.* 115 (2015), 235502.
- [13] K. Matsunaga, M. Yoshiya, N. Shibata, H. Ohta, T. Mizoguchi, Ceramic science of crystal defect cores, *J. Ceram. Soc. JAPAN* 130 (8) (2022) 648–667.
- [14] J.R. Morris, Z.-Y. Lu, D.M. Ring, J.-B. Xiang, K.-M. Ho, C.Z. Wang, First-principles determination of the  $\Sigma = 13(510)$  symmetric tilt boundary structure in silicon and germanium, *Phys. Rev. B* 58 (1998) 11241–11245.
- [15] M. Kohyama, Computational studies of grain boundaries in covalent materials, *Model. Simulat. Mater. Sci. Eng.* 10 (2002) 31–59.
- [16] J. Zhang, C.-Z. Wang, K.-M. Ho, Finding the low-energy structures of Si[001] symmetric tilted grain boundaries with a genetic algorithm, *Rhys. Rev. B* 80 (2009), 174102.
- [17] L. Wang, W. Yu, S. Shen, Revisiting the structures and energies of silicon <110> symmetric tilt grain boundaries, *J. Mater. Res.* 34 (2019) 1021–1033.
- [18] J.D. Rittner, D.N. Seidman, 110> symmetric tilt grain-boundary structures in fcc metals with low stacking-fault energies, *Phys. Rev. B* 54 (1996) 6999–7015.
- [19] M.A. Tschopp, D.L. McDowell, Asymmetric tilt grain boundary structure and energy in copper and aluminium, *Philos. Mag. A* 87 (2007) 3871–3892.
- [20] D.L. Olmsted, S.M. Foiles, E.A. Holm, Survey of computed grain boundary properties in face-centered cubic metals: I. Grain boundary energy, *Acta Mater.* 57 (2009) 3694–3703.
- [21] E.N. Hahn, S.J. Fensin, T.C. German, M.A. Meyers, Symmetric tilt boundaries in body-centered cubic tantalum, *Scripta Mater.* 116 (2016) 108–111.
- [22] J.H. Harding, D.J. Harris, Computer simulation of general grain boundaries in rocksalt oxides, *Phys. Rev. B* 60 (1999) 2740–2746.
- [23] M. Yoshiya, T. Oyama, Impurity and vacancy segregation at symmetric tilt grain boundaries in  $Y_2O_3$ -doped  $ZrO_2$ , *J. Mater. Sci.* 46 (2011) 4176–4190.
- [24] H. Guhl, H.-S. Lee, P. Tangney, W.M.C. Foulkes, A.H. Heuer, T. Nakagawa, Y. Ikuhara, M.W. Finnis, Structural and electronic properties of  $\Sigma 7$  grain boundaries in  $\alpha\text{-Al}_2\text{O}_3$ , *Acta Mater.* 99 (2015) 16–28.
- [25] T. Frolov, W. Setyawati, R.J. Kurtz, J. Marian, A.R. Oganov, R.E. Rudd, Q. Zhu, Grain boundary phases in bcc metals, *Nanoscale* 10 (2018) 8253–8268.
- [26] Q. Zhu, A. Samanta, B. Li, R.E. Rudd, T. Frolov, Predicting phase behavior of grain boundaries with evolutionary search and machine learning, *Nat. Commun.* 9 (2018) 467.
- [27] T. Frolov, Q. Zhu, T. Oppelstrup, J. Marian, R.E. Rudd, Structures and transitions in bcc tungsten grain boundaries and their role in the absorption of point defects, *Acta Mater.* 159 (2018) 123–134.
- [28] J.-S. Park, Self-passivation rule and structure of CdTe  $\Sigma 3(112)$  grain boundaries, *Phys. Rev. Mater.* 3 (2019), 014602.
- [29] C. Yang, M. Zhang, L. Qi, Grain boundary structure search by using an evolutionary algorithm with effective mutation methods, *Comput. Mater. Sci.* 184 (2020), 109812.
- [30] T. Yokoi, K. Kondo, K. Ikawa, A. Nakamura, K. Matsunaga, Stable and metastable structures and their energetics of asymmetric tilt grain boundaries in MgO: a simulated annealing approach, *J. Mater. Sci.* 56 (2021) 3183–3196.
- [31] N.A. Benedek, A.L.S. Chua, C. Elsässer, A.P. Sutton, M.W. Finnis, Interatomic potential for strontium titanate: an assessment of their transferability and comparison with density functional theory, *Phys. Rev. B* 78 (2008), 064110.
- [32] T. Yokoi, K. Adachi, S. Iwase, K. Matsunaga, Accurate prediction of grain boundary structures and energetics in CdTe: a machine-learning interatomic potential, *Phys. Chem. Chem. Phys.* 24 (2021) 1620–1629.
- [33] J. Behler, M. Parrinello, Generalized neural-network representation of high-dimensional potential-energy surface, *Phys. Rev. Lett.* 98 (2007), 146401.
- [34] A.P. Bartók, M.C. Payne, R. Kondor, G. Csányi, Gaussian approximation potentials: the accuracy of quantum mechanics, without the electrons, *Phys. Rev. Lett.* 104 (2010), 136403.
- [35] J. Behler, Neural network potential-energy surfaces in chemistry: a tool for large-scale simulations, *Phys. Chem. Chem. Phys.* 13 (2011) 17930–17955.
- [36] J. Behler, Constructing high-dimensional neural network potentials: a tutorial review, *Int. J. Quant. Chem.* 115 (2015) 1032–1050.
- [37] A.P. Bartók, G. Csányi, Gaussian approximation potentials: a brief tutorial introduction, *Int. J. Quant. Chem.* 115 (2015) 1051–1057.
- [38] T. Mueller, A. Hernandez, C. Wang, Machine learning for interatomic potential models, *J. Chem. Phys.* 152 (2020), 050902.
- [39] Y. Mishin, Machine-learning interatomic potentials for material science, *Acta Mater.* 214 (2021), 116980.
- [40] D. Dragoni, T.D. Daff, G. Csányi, N. Marzari, Achieving DFT accuracy with a machine-learning interatomic potential: thermomechanics and defects in bcc ferromagnetic iron, *Phys. Rev. B* 2 (2018), 013808.
- [41] A.S. Bochkarev, A. van Roekeghem, S. Mossa, N. Mingo, Anharmonic thermodynamics of vacancies using a neural network potential, *Phys. Rev. Mater.* 3 (2019), 093803.
- [42] J. Byggmästar, A. Hamedani, K. Nordlund, F. Djurabekova, Machine-learning interatomic potential for radiation damage and defects in tungsten, *Phys. Rev. B* 100 (2019), 14405.
- [43] H. Babaei, R. Guo, A. Hashemi, S. Lee, Machine-learning-based interatomic potential for phonon transport in perfect crystalline Si and crystalline Si with vacancies, *Phys. Rev. Mater.* 3 (2019), 074603.
- [44] J. Byggmästar, K. Nordlund, F. Djurabekova, Gaussian approximation potentials for body-centered-cubic transition metals, *Phys. Rev. Mater.* 4 (2020), 093802.
- [45] S.K. Natarajan, J. Behler, Neural network molecular dynamics simulations of solid-liquid interfaces: water at low-index copper surfaces, *Phys. Chem. Chem. Phys.* 18 (2016), 28704.

- [46] A.P. Bartók, J. Kermode, N. Bernstein, G. Csányi, Machine learning a general-purpose interatomic potential for silicon, *Phys. Rev. X* 8 (2018), 041048.
- [47] R. Kobayashi, D. Giofré, T. Junge, M. Ceriotti, W.A. Curtin, Gaussian approximation potentials for body-centered-cubic transition metals, *Phys. Rev. Mater.* 1 (2017), 053604.
- [48] H. Mori, T. Ozaki, Neural network atomic potential to investigate the dislocation dynamics in bcc iron, *Phys. Rev. Mater.* 4 (2020), 040601.
- [49] Y. Wang, J. Liu, J. Li, J. Mei, Z. Li, W. Lai, F. Xue, Machine-learning interatomic potential for radiation damage effects in bcc-iron, *Comput. Mater. Sci.* 202 (2022), 110960.
- [50] D. Lanzoni, F. Rovaris, F. Montalenti, Machine learning potential for interacting dislocations in the presence of free surfaces, *Sci. Rep.* 12 (2022) 3760.
- [51] T. Yokoi, Y. Noda, A. Nakamura, K. Matsunaga, Neural-network interatomic potential for grain boundary structures and their energetics in silicon, *Phys. Rev. Mater.* 4 (2020), 014605.
- [52] T. Nishiyama, A. Seko, I. Tanaka, Application of machine learning potentials to predict grain boundary properties in fcc elemental metals, *Phys. Rev. Mater.* 4 (2020), 123607.
- [53] Y. Shiiroha, R. Kanazawa, D. Matsunaka, I. Lobzenko, T. Tsuru, M. Kohyama, H. Mori, Artificial neural network molecular mechanics of iron grain boundaries, *Scripta Mater.* 207 (2022), 114268.
- [54] P.E. Elöchl, Projector augmented-wave method, *Phys. Rev. B* 50 (1994) 17953–17979.
- [55] G. Kresse, D. Joubert, From ultrasoft pseudopotentials to the projector augmented-wave method, *Phys. Rev. B* 19 (1999) 1758–1775.
- [56] G. Kresse, J. Furthmüller, Efficiency of ab-initio total energy calculations for metals and semiconductors using a plane-wave basis set, *Comput. Mater. Sci.* 6 (1996) 15–50.
- [57] G. Kresse, J. Furthmüller, Efficient iterative schemes for ab initio total-energy calculations using a plane-wave basis set, *Phys. Rev. B* 54 (1996) 11169–11186.
- [58] J.P. Perdew, A. Ruzsinszky, G.I. Csonka, O.A. Vydrov, G.E. Scuseria, L. A. Constantin, X. Zhou, K. Burke, Restoring the density-gradient expansion for exchange in solids and surfaces, *Phys. Rev. Lett.* 100 (2008), 136406.
- [59] M. Parrinello, A. Rahman, Crystal structure and pair potentials: a molecular-dynamics study, *Phys. Rev. Lett.* 45 (1980) 1196–1199.
- [60] M. Parrinello, A. Rahman, Polymorphic transitions in single crystals: a new molecular dynamics method, *J. Appl. Phys.* 52 (1981) 7182–7190.
- [61] T.B. Blank, S.D. Brown, Adaptive, global, extended Kalman filters for training feedforward neural networks, *J. Chemom.* 8 (1994) 391–407.
- [62] S. von Alftan, P.D. Haynes, K. Kaski, A.P. Sutton, Are the structures of twist grain boundaries in silicon ordered at 0 K? *Phys. Rev. Lett.* 96 (2006), 055505.
- [63] H. Sawada, H. Ichinose, Structure of {112} Σ3 boundary in silicon and diamond, *Scripta Mater.* 44 (2001) 2327–2330.
- [64] J. Tersoff, Empirical interatomic potential for silicon with improved elastic properties, *Phys. Rev. B* 38 (1988) 9902–9905.
- [65] J. Tersoff, Modeling solid-state chemistry: interatomic potentials for multicomponent systems, *Phys. Rev. B* 39 (1989) 5566–5568.
- [66] S. Plimpton, Fast parallel algorithms for short-range molecular dynamics, *J. Comp. Physiol.* 117 (1995) 1–19.
- [67] J.D. Gale, GULP: a computer program for the symmetry-adapted simulation of solids, *J. Chem. Soc., Faraday Trans.* 93 (1997) 629–637.
- [68] N. Artrith, J. Behler, High-dimensional neural network potentials for metal surfaces: a prototype study for copper, *Phys. Rev. B* 85 (2012), 045439.
- [69] N. Artrith, A. Urban, An implementation of artificial neural-network potentials for atomistic materials simulations: performance for TiO<sub>2</sub>, *Comput. Mater. Sci.* 114 (2016) 135–150.

## Update

**Journal of Physics and Chemistry of Solids**

Volume 176, Issue , May 2023, Page

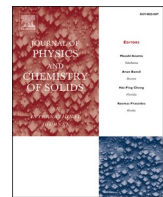
DOI: <https://doi.org/10.1016/j.jpcs.2023.111273>



Contents lists available at ScienceDirect

## Journal of Physics and Chemistry of Solids

journal homepage: [www.elsevier.com/locate/jpcs](http://www.elsevier.com/locate/jpcs)



### Corrigendum to “Atomic structures of grain boundaries for Si and Ge: A simulated annealing method with artificial-neural-network interatomic potentials” [J. Phys. Chem. Solid. 173 (2023) 111114]

Tatsuya Yokoi <sup>a,\*</sup>, Hirotaka Kato <sup>a</sup>, Yu Oshima <sup>a</sup>, Katsuyuki Matsunaga <sup>a,b</sup>

<sup>a</sup> Department of Materials Physics, Nagoya University, Nagoya, 464-8603, Japan

<sup>b</sup> Nanostructures Research Laboratory, Japan Fine Ceramics Center, Nagoya, 456-8587, Japan



The authors regret the inclusion of author Hirotaka Kato. Professor Hirotaka Kato name has been removed from the article.

The authors would like to apologise for any inconvenience caused.

DOI of original article: <https://doi.org/10.1016/j.jpcs.2022.111114>.

\* Corresponding author.

E-mail address: [yokoi@mp.pse.nagoya-u.ac.jp](mailto:yokoi@mp.pse.nagoya-u.ac.jp) (T. Yokoi).